New Method for Investigating Crack Development in Concrete Using an Ultrahigh-Speed Camera

Xianwei Zhang[1]; Shouyi Li, Ph.D.[2]; Yuan Qin, Ph.D.[3]; Junrui Chai, Ph.D.[4]; Zengguang Xu, Ph.D.[5]; and Zheng Si, Ph.D.[6]

Abstract: Cracks are ubiquitous in concrete materials and can destabilize a concrete structure, regardless of size or type. This study focuses on the cracking behavior of main and branching cracks in concrete. Compression tests and an ultrahigh-speed camera are utilized to capture the crack formation. Crack length and cracking speed under a compressive load are measured and calculated. An accurate method for measuring crack characteristics is presented. Results show that the length–time and developing speed–time curves of the branching crack exhibit an evident fluctuation compared with that of the main crack. The main crack maintained a relatively stable crack development speed during the entire loading process. This relatively stable speed may result from the development of the branching crack. If the concrete is damaged, then the branching crack can delay the cracking speed of the main crack and minimize damage. **DOI: 10.1061/(ASCE)MT.1943-5533.0002578.**

Author keywords: Concrete; Crack; High-speed camera; Ultrahigh-speed camera.

Introduction

Concrete is a quasi-brittle material (Galouei and Fakhimi 2015; Pichler and Hellmich 2011; Gary and Bailly 1998) widely used in civil engineering (Li et al. 2012; Lai et al. 2017, 2018; Zhou et al. 2014; Tarefder and Ahmad 2015), water conservation (Soumya Pandey et al. 2016; Agoramoorthy 2015), and other national key engineering projects (Oey et al. 2014; Yang et al. 2018; Palankar et al. 2016; Faella et al. 2016; Damasceno et al. 2013; Qiu et al. 2018a, b). The fracture strength of this material fluctuates and changes under different test conditions, e.g., temperature, chemical environment, and load rate, thereby resulting in further systematic variations in strengths (Lawn 1993). Thus, the universal validity of the critical applied stress thesis has become unreliable (Lawn 1993). In general, energy will accumulate in concrete under an external load, and cracks will appear when this energy exceeds a certain limit after it has undergone the conversion process from micro to macro (Lawn 1993; Yu et al. 2016). Microcracks always form in the interior of the concrete, with the absorbed energy gradually evolving into macrocracks (small or large cracks on the surface of concrete), which can be detected by human eyes (Qin et al. 2013). Macrocracks also evolve into main and branching cracks.

Regardless of crack form or size, cracks will break the continuity and integrity of a concrete specimen or structure, thereby leading to instability (Qin et al. 2016). However, the authors determined that if main cracks have already appeared in concrete, then branching cracks may stabilize the structure by delaying the development speed of large cracks. This phenomenon is interesting. The relationship between formation speed of main and branching cracks should be established to investigate this phenomenon. Traditional methods such as computed tomography, acoustic emission, ultrasound, and infrared spectroscopy exhibit limitations in investigating the rapid changes on the surface of a concrete structure. Thus, a high-speed measurement method is necessary.

High-speed cameras (HSCs) and ultrahigh-speed cameras (UHSCs) are basic equipment for rapid measurements. Fig. 1 shows the work of Reu and Miller (2008), which indicated a large gap between the frame rate and recording length of HSCs and UHSCs. For example, at 100,000 frames per second (FPS) [number of pictures (frames) taken per second; the x-axis in Fig. 1], i.e., 100,000 pictures (y-axis), the picture resolution of HSCs will be reduced to 256×256 pixels; i.e., fast speed results in the low spatial resolution of HSCs. A HSC can provide 100,000 FPS (x-axis) with recording lengths of approximately 90,000 pictures (y-axis), whereas UHSCs can provide at least 100,000 FPS (x-axis) with recording lengths of only 100 pictures (y-axis), i.e., fast speed results in the short recording length of UHSCs. In recent years, however, HSC and UHSC technologies have improved significantly (Fig. 2).

In Fig. 1, the pink zone in the work of Reu and Miller (2008) is called "no camera technologies available." However, several UHSCs can shoot 180 or even more images with FPS values between 1,000 and 1 million and maintain 924×768 pixels. This technology provides a clear picture and high shoot speed for the experiment.

[1]Ph.D. Candidate, State Key Laboratory of Eco-Hydraulics in Northwest Arid Region of China, Xi'an Univ. of Technology, Xi'an 710048, China. Email: grace0877@163.com

[2]Professor, State Key Laboratory of Eco-Hydraulics in Northwest Arid Region of China, Xi'an Univ. of Technology, Xi'an 710048, China. Email: lishouyi@126.com

[3]Associate Professor, State Key Laboratory of Eco-Hydraulics in Northwest Arid Region of China, Xi'an Univ. of Technology, Xi'an 710048, China (corresponding author). Email: lanelyly@163.com; qinyuan@xaut.edu.cn

[4]Professor, State Key Laboratory of Eco-Hydraulics in Northwest Arid Region of China, Xi'an Univ. of Technology, Xi'an 710048, China. Email: jrchai@xaut.edu.cn

[5]Associate Professor, State Key Laboratory of Eco-Hydraulics in Northwest Arid Region of China, Xi'an Univ. of Technology, Xi'an 710048, China. Email: xuzengguang@xaut.edu.cn

[6]Associate Professor, State Key Laboratory of Eco-Hydraulics in Northwest Arid Region of China, Xi'an Univ. of Technology, Xi'an 710048, China. Email: sz123hlz@163.com

Note. This manuscript was submitted on December 11, 2017; approved on July 24, 2018; published online on November 10, 2018. Discussion period open until April 10, 2019; separate discussions must be submitted for individual papers. This paper is part of the ***Journal of Materials in Civil Engineering***, © ASCE, ISSN 0899-1561.

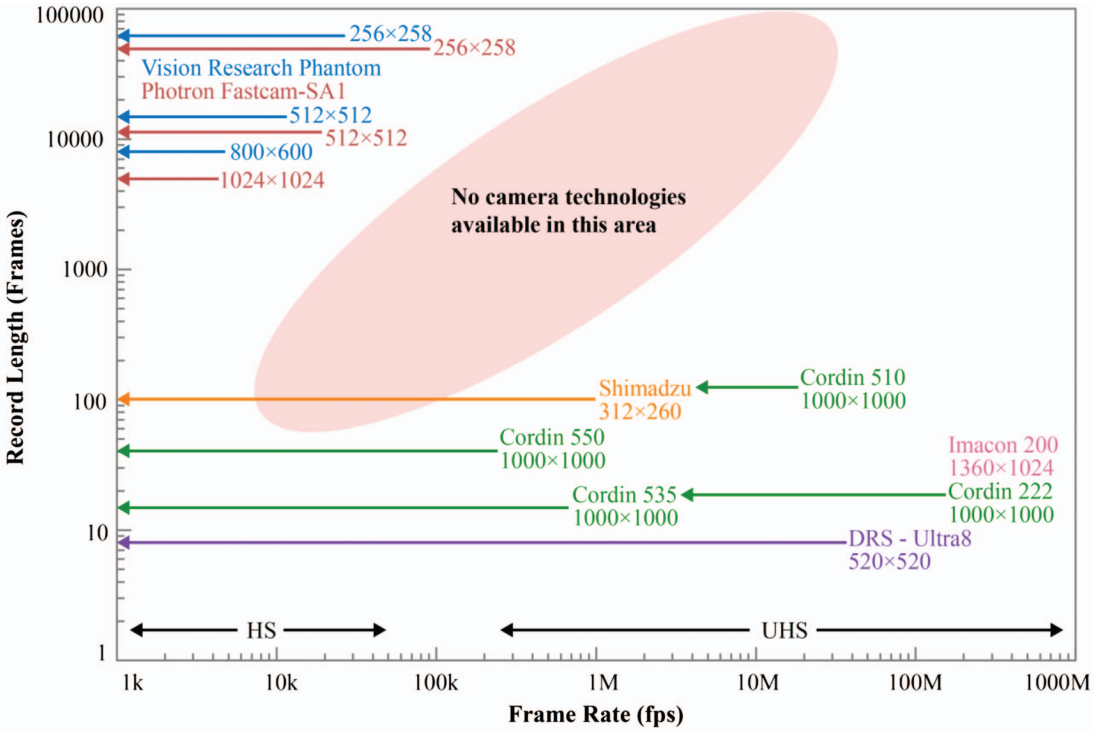

Fig. 1. (Color) Survey of HSC imaging technology. (Data from Reu and Miller 2008.)

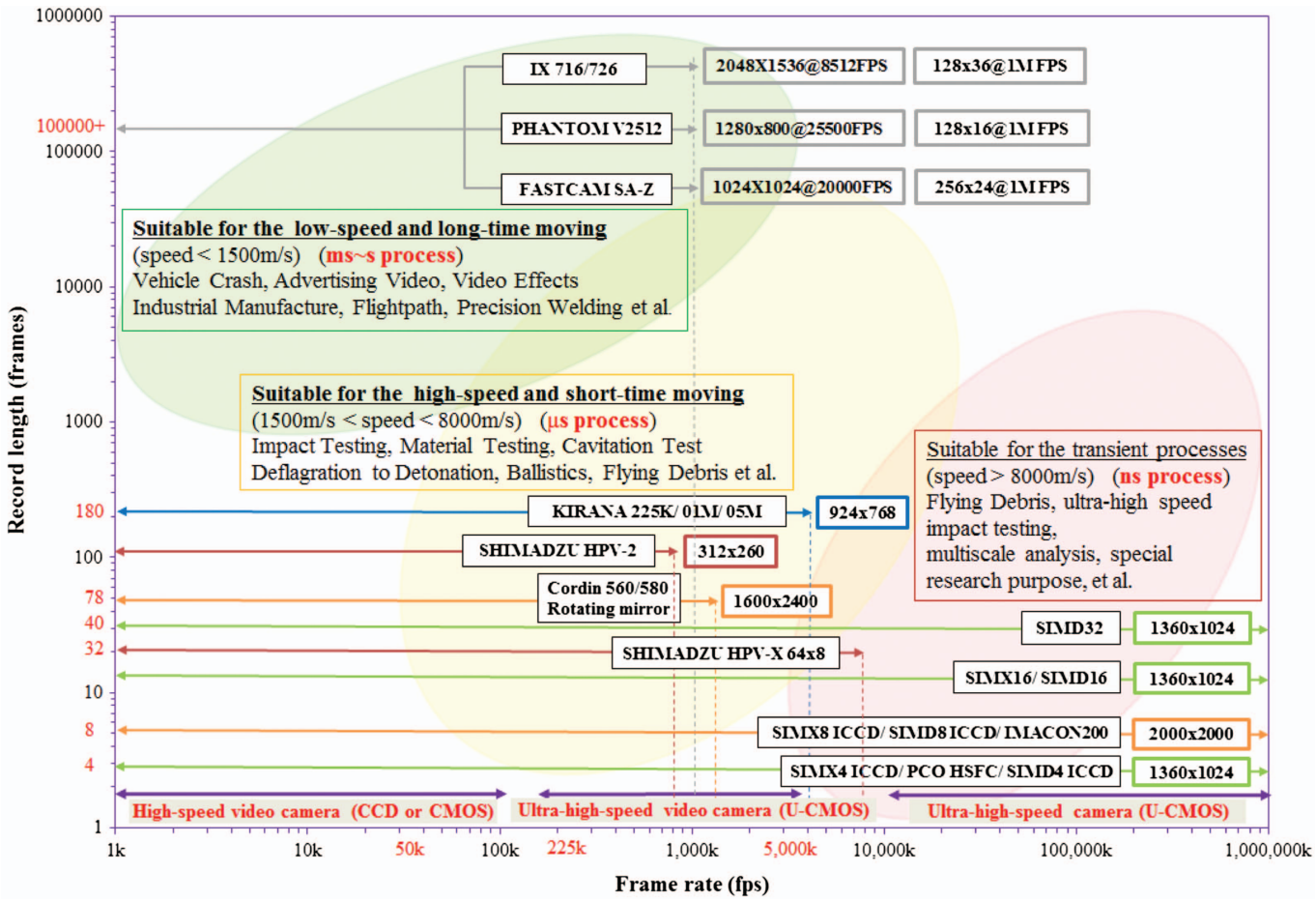

Fig. 2. (Color) Primary survey of HSCs and UHSCs used in scientific research. Maximum resolution along with the recording lengths (y-axis) and rates (x-axis) are shown.

Table 1. HSCs and UHSCs used in crack propagation tests

Number	Material	Model size (mm)	Load	Camera	References
1	High-performance concrete	$L = 223$, $B = 25$, $H = 76$	Hydraulic and impact	HSC	Pyo et al. (2016)
2	Steel-fiber-reinforced concrete with short glass fiber	$L = 50$, $B = 25$, $H = 10$	Hydraulic	HSC	Yao et al. (2015)
3	Concrete with hard siliceous aggregates with grain sizes of 2–8 mm	$L = 120$, $B = 60$, $H = 20$	Hydraulic	UHSC	Forquin (2012)

Table 2. HSCs and UHSCs used in projectile impact tests

Number	Material	Model size (thickness in mm)	Load speed of projectile (m/s)	Camera	References
1	Concrete	400, 800	620	HSC	Unosson and Nilsson (2006)
2		300, 400, 500, 600, 700	400	HSC	Li et al. (2013)
3		100, 150, 200, 300	536–737	HSC	Wu et al. (2015)
4		100	830	Two HSCs	Yu et al. (2016)
5		400	400, 600	HSC	Wang et al. (2016)
6		60–80	190–420	HSC	Ueno et al. (2017)

Table 3. HSCs and UHSCs used in SHPB tests

Number	Material	Model size (thickness in mm)	Load	Camera	References
1	Marble	20	Dynamic	HSC and macro lens	Zhang and Zhao (2013)
2	Granite	—	Quasi-static and dynamic	HSC	Xu et al. (2015)
3	Rock	16	Dynamic	UHSC	Gao et al. (2015)
4	Granite	50	Quasi-static and dynamic	HSC	Zhou et al. (2017)

Many researchers have already used HSCs and UHSCs in concrete cracking studies (Matthes et al. 2016; Scalici et al. 2015; Destrebecq et al. 2011; Küntz et al. 2006; Wu et al. 2011; Aggelis et al. 2013; Nunes and Reis 2012; Li et al. 2016; Wu et al. 2016). However, given the complex internal structures of concrete, the relationship between main and branching cracks remains inadequately understood. Concrete experiments using HSCs or UHSCs have mainly included crack propagation tests, projectile impact tests, and the split Hopkinson pressure bar (SHPB) test.

For crack propagation tests, Pyo et al. (2016) used a HSC and edge detection technology to analyze crack propagation speed in ultrahigh-performance concrete. Yao et al. (2015) added short glass fibers to reinforced concrete to test tension stiffening via a HSC. The width of a crack was captured by the HSC. Five stress-strain curves of the specimen and their characteristic cracks were obtained under different loading rates. Forquin (2012) investigated concrete spalling with a specimen that contained wet and dry saturated concrete. A strain gauge and UHSC were coupled and used simultaneously. Table 1 lists the data from these three aforementioned studies, including the kind of concrete, concrete model size, and camera type.

For projectile impact tests, Unosson and Nilsson (2006) tested a 620-m/s projectile that struck different thicknesses of concrete. The process was tracked and measured using a HSC and Doppler radar. The residual velocity of the projectile was calculated. Li et al. (2013) used a projectile to strike different thicknesses of concrete at a constant speed of 400 m/s. A HSC was used to photograph the penetration events. Wu et al. (2015) used a projectile to strike different thicknesses of concrete at speeds of 536–737 m/s. The impact was monitored using a HSC. Yu et al. (2016) introduced a HSC into a high-speed bullet impact test (speed of 830 m/s) to detect the energy absorption of ultrahigh-performance concrete in quasi-static mode. Wang et al. (2016) used a 0.25-kg projectile with a diameter of 28 mm and speeds of 400–600 m/s to strike concrete slabs. The dynamic process was monitored with a HSC. Ueno et al. (2017) used a 10,000 FPS HSC to record the projectile impact on steel-fiber concrete. Detailed information on the aforementioned experiments is provided in Table 2.

The SHPB test has a 60-year history. This test mainly focuses on the mechanical properties of concrete under a high strain rate. This method is widely used in the research of concrete, rock, and ceramics. It is frequently adopted to test the mechanical properties of concrete under projectiles/bullets, explosions, and other high-rate loading events. Zhang and Zhao (2013) combined SHPB and a HSC to analyze the mechanical properties of rocks, including crack growth toughness, dynamic tensile strength, and dynamic uniaxial compressive strength. Xu et al. (2015) used a HSC to record the experimental process of granite during a SHPB test based on a new shear-loading technique. Gao et al. (2015) used a UHSC to record the fracture processes on an oblique surface of a notched semicircular bend specimen under normal and shear stresses. Zhou et al. (2017) investigated the microprocess and inner mechanism of rock failure under impact loading based on a SHPB test and recorded the experimental process with a 10,000 FPS HSC. Detailed information on the aforementioned experiments is provided in Table 3.

In the present study, the cracking behavior of main and branching cracks in concrete is investigated based on a self-made trigger system. Compression tests were conducted on concrete specimens, and a UHSC was used to capture crack formation, crack length, and cracking speed under a compressive load. An accurate method for measuring crack characteristics is presented.

Compression Experiment

Experimental Setup

The concrete material compression test used a concrete specimen, UHSC, computers, connection system (line system), light source,

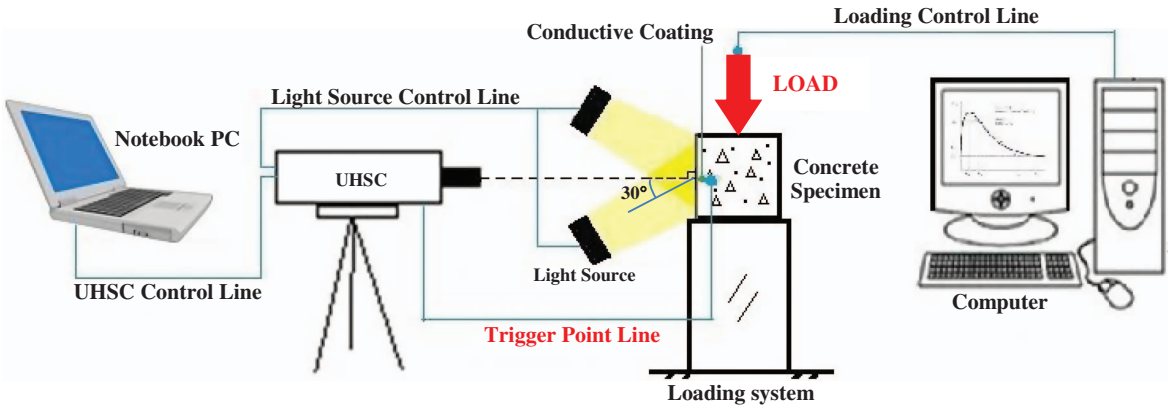

(a)

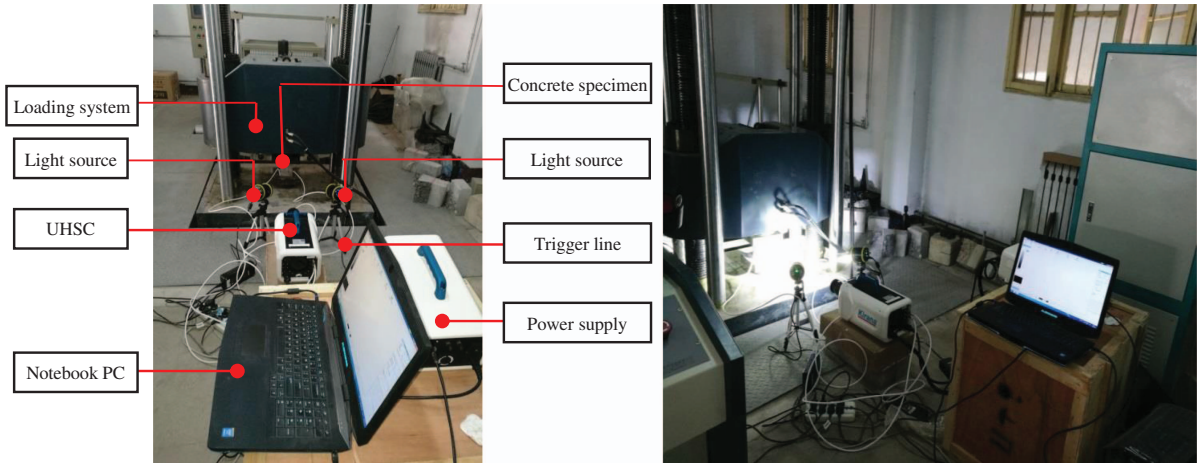

(b)

Fig. 3. (Color) (a) Experimental setup; and (b) system used in the experiment.

and loading system. The experimental setup is shown in Fig. 3(a), and the system is presented in Fig. 3(b). The main parameters of the UHSC are listed in Table 4. This experiment requires two computers: one that controls the UHSC and another that controls the loading system. The light source is a light-emitting diode (LED) bulb because it is a low-voltage direct current (DC) light. An alternating current (AC) light will result in a flickering video.

Trigger System

The most important device in this system is the trigger system, which was constructed by the authors. The trigger system contains a trigger point line and conductive coating. Fig. 4(a) shows the principle diagram of the trigger system. The trigger point line is a coaxial cable, with one end fixed to the UHSC and the other end fixed to a concrete specimen. A detailed link method is illustrated in Fig. 4(b). The conductive coating can be a graphite mixture solution or copper–silver mixture solution. The electrical conductivity results show that although the graphite mixture solution is better than the copper–silver mixture solution, it exhibits poor concrete adhesive capability. Thus, the copper–silver mixture solution was selected as the conductive coating. In the experiment, the conductive coating is similar to a starting line of the crack. The timer and UHSC shooting will start when the crack exceeds this starting line.

The width of the conductive coating in this experiment ranged from 4 to 6 mm. A narrow conductive coating is required, but an extremely narrow conductive coating will lead to a flawed contact in the trigger system. For example, failure rates of the trigger system and experiment will increase when the width of the conductive coating is less than 4 mm. Similarly, an extremely wide coating will also lead to the increase in failure rates. An excessively wide coating will require much time to cut off. Moreover, the self-made sensor [Fig. 4(c)] may have poor contact with the end of the conductive coating during a long cutting-off time. This phenomenon also directly leads to an increase in failure rates. By contrast, the conductive coating will influence the total length of Crack 2 (the definition of Crack 2 is provided in the "Experimental Results and Analysis" section) but will not influence the test result of the unit length of the crack when the width of the conductive coating exceeds 6 mm. Thus, the width of the conductive coating will slightly influence the test result of the development speed of the crack. The instantaneous velocity is calculated by unit length divided by unit time

Table 4. Main parameters of the UHSC used in the experiment

Parameter	Value
Frame rate	1 million FPS
Record number	180 frames (pictures)
Image resolution ratio	768 $(H) \times 924$ (W)
Exposure time	1 ms–100 ns
Sensor structure	μCMOS
Pixel size	30 μm

Note: CMOS = complementary metal oxide semiconductor.

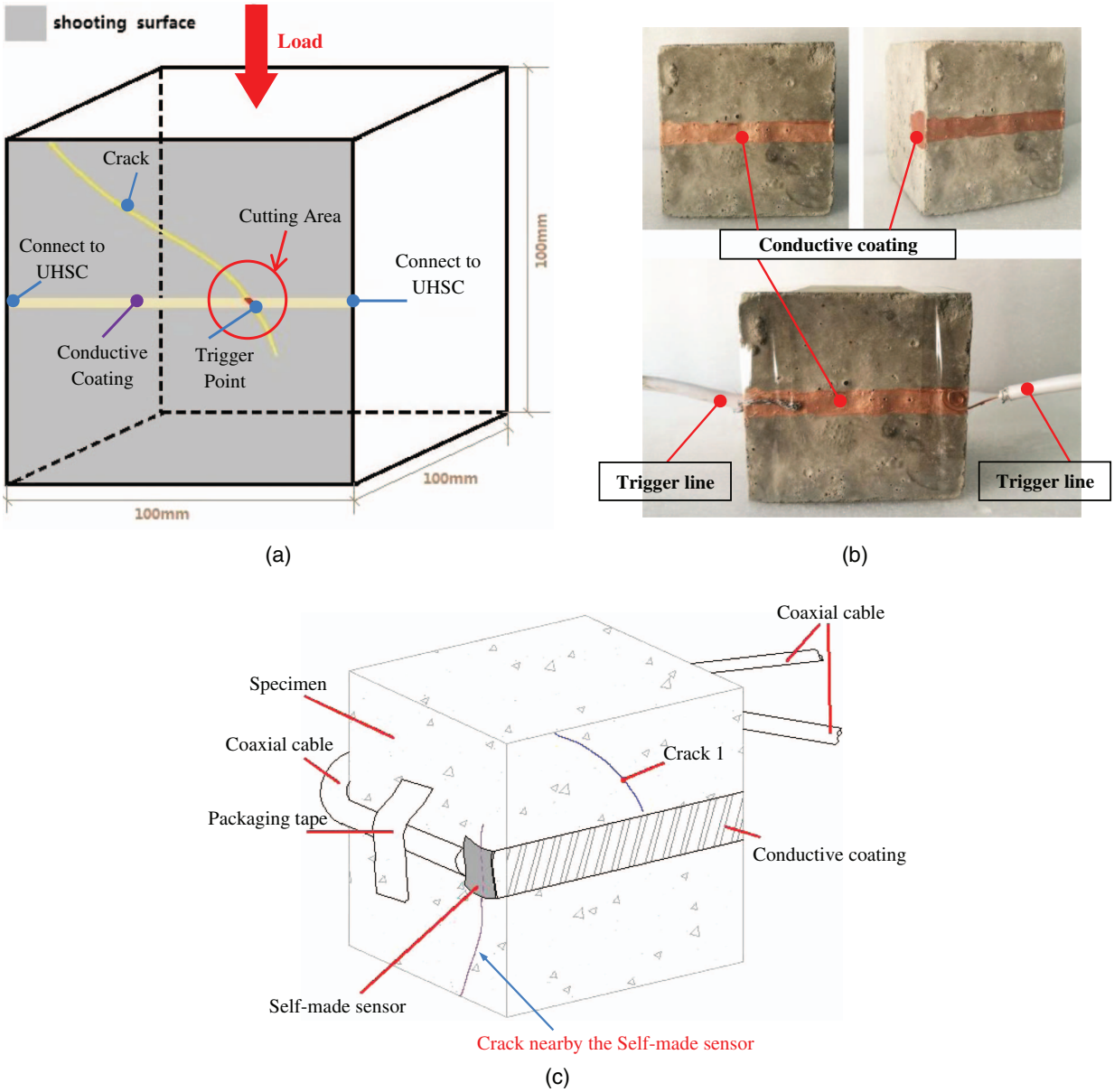

Fig. 4. (Color) (a) Principle diagram of the trigger system; (b) system and detailed drawing of the connection; and (c) self-made sensor connected with conductive coating.

because this development speed is an instantaneous velocity of the crack.

Additionally, if the crack does not cross the conductive coating, then this scenario may be explained by the appearance of the crack near the self-made sensor. The trigger system was effective when a crack appeared near the self-made sensor; however, a crack did not cut the conductive coating at that time [Fig. 4(c)]. This phenomenon suggests a test failure because the crack did not cross the conductive coating. Simultaneously, the experimental results indicate that a crack constantly generates the effect of energy release when this crack appears. Thus, the crack will continuously develop with the load and eventually result in a cut-off from the conductive coating when this crack appears in the shooting surface. In this experiment, it was assumed that the width of cracks had a constant value, and the small cracks were ignored given the limitation of the resolution ratio of the UHSC. This experimental gap may be a key point of a future work.

Experimental Procedure

The experimental procedure includes the specimen test, trigger system test, UHSC system test, and loading/data acquisition (Fig. 5 shows a flowchart). The mixture design of the concrete specimens is presented in Table 5. In preparing the specimens, the aggregate, sand, and cement were first placed in an agitator and stirred for 2 min. Then, water was poured into the mixture at three different times. After this step, the mixture was stirred for 3 min, placed in a mold, and vibrated for 15–20 s. Then, the mold filled with unset concrete was placed in a curing box for 24 h, followed by the removal of the mold. The concrete specimen was cured in the curing box for 28 days. Three specimens were investigated in the experiment. These specimens were labeled Specimen 1 through Specimen 3. The specimens had the same geometry ($100 \times 100 \times 100$ mm), mix design, and curing conditions (curing temperature was kept constant at $20°C \pm 2°C$ and humidity not lower than 95%).

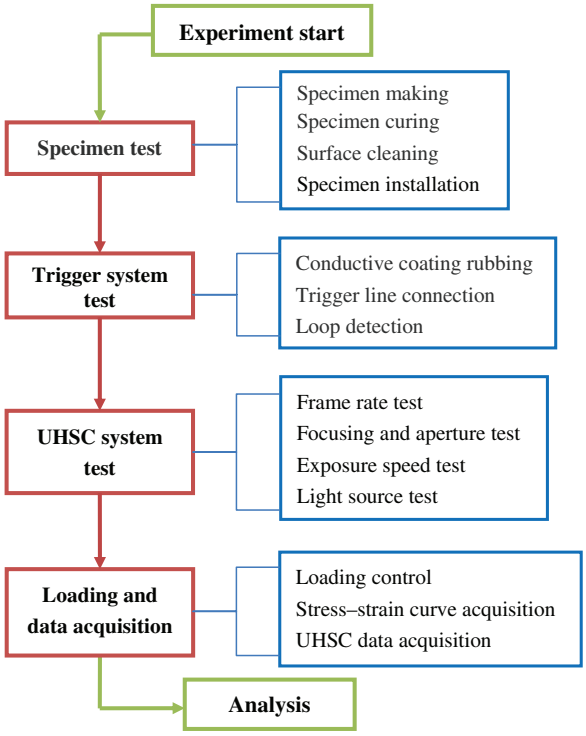

Fig. 5. (Color) Experiment flowchart.

Table 5. Mixture design of the concrete specimen

Parameter	Value
Water-to-binder ratio	0.4
Sand-to-aggregate weight ratio	0.31
Unit weight (kg/m^3)	—
Water	120
Cement	225
Fly ash	75
Sand	614
5–10 mm gravel	546
10–30 mm gravel	820
Air-entraining agent	0.135
Superplasticizer	2.1

In the trigger system test stage, the shooting surface should be cleaned first and rubbed with the conductive coating. Although each specimen had six faces, only one of these faces was selected as the shooting face in the experiment. Second, the trigger line was attached to both ends of the conductive coating. Third, the entire circuit of the trigger system was checked and ensured to be unimpeded.

Then, the focus and aperture, exposure speed, and light source tests were conducted before every experiment. The frame rate was determined as 1,000 FPS, and the aperture was confirmed to be wide. The exposure speed was 1 ms, and the incident angle of the light source was 30°. Finally, a loading apparatus was used to apply a load to the specimen and record the stress-strain curves and crack videos.

Experiment Results and Analysis

Qualitative Analysis

Instantaneous pictures within 180 ms after the cracks cut off the conductive coating of Specimen 1 were collected. Fig. 6(a) displays the picture of $t = 90$ ms of Specimen 1 (two sides of the specimen have a transparent adhesive tape; the transparent adhesive tape is bright because it is reflective). The left side of the specimen exhibits a thin crack at this time. For a clear analysis, an inverted picture of the crack is depicted in Fig. 6(b). A sketch map of the crack is presented in Fig. 6(c). In Fig. 6(c), all the cracks are divided into three parts as follows: Main crack 1 (before the trigger point), Main crack 2 (after the trigger point), and the branching crack. The UHSC will capture images after Main crack 1 cuts off the conductive coating.

Fig. 7 shows several pictures of Specimens 1–3 at $t = 15$, 30, 45, 90, 120, 140, 160, and 179 ms (serial numbers of the pictures range from 0 to 179) to describe the crack development process. Fig. 7 demonstrates that the crack locations are random in different specimens. However, certain characteristics (e.g., length of Main crack 2 of each specimen) similar to each other gradually increased within 180 ms after Main crack 1 had cut off the conductive coating and the direction of Main crack 2 of all specimens shifted from the middle to the bottom of the specimen. A branching crack appeared at $t = 15$, 45, and 30 ms of Specimen 1, Specimen 2, and Specimen 3, respectively. Main crack 2 had continuously developed toward the bottom of the specimen during the entire branching crack development time. The direction of the crack shifted from the middle

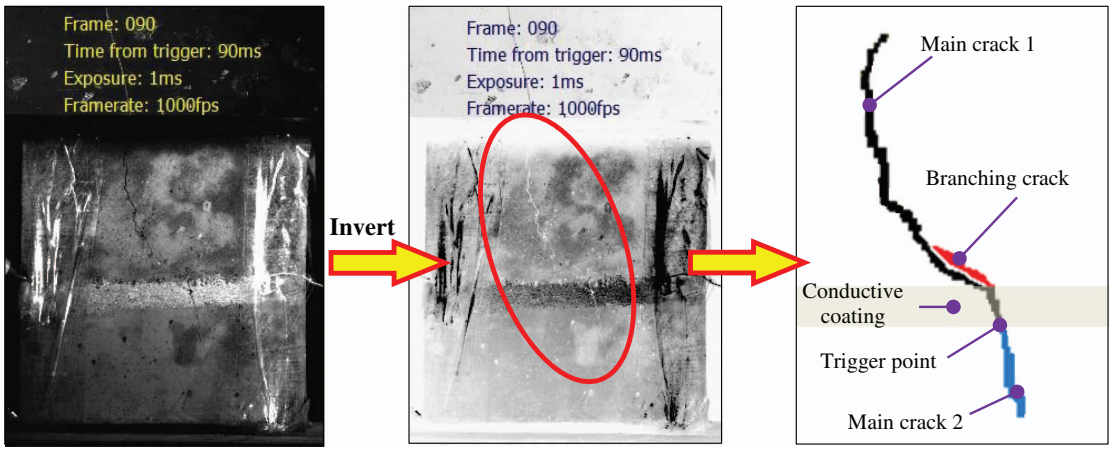

Fig. 6. (Color) (a) Picture taken at $t = 90$ ms; (b) its inverted picture; and (c) definition of cracks.

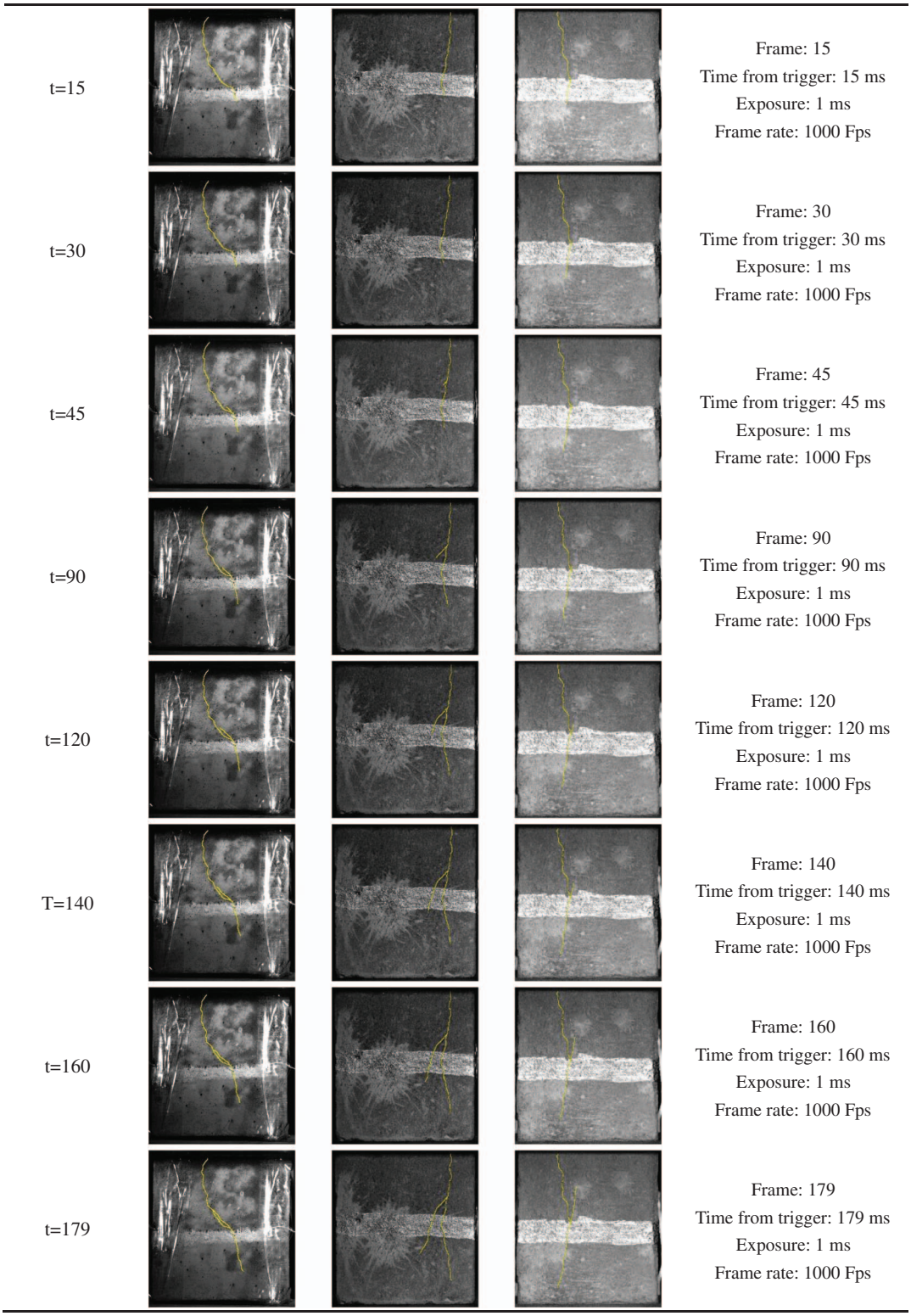

Fig. 7. (Color) UHSC pictures at $t = 15$, 30, 45, 90, 120, 140, 160, and 179 ms for Specimens 1, 2, and 3.

to the top of Specimens 1 and 3, but the direction of the crack shifted from the top to the middle of Specimen 2. This phenomenon was due to the random inner structure of the concrete materials.

Quantitative Analysis

Each crack length was measured by spline (SPL) in AutoCAD (version 2014). The measurement method was based on the river length measurement principle in engineering, and the findings are summarized in Table 6 for investigating the relationship of the crack lengths between Main crack 2 and the branching crack of Specimens 1–3. For example, in Specimen 1, the length of Main crack 1 remained $L_{m1} = 72.64$ mm and did not change throughout $t = 0$–179 ms because it already existed before the UHSC shooting. After Main crack 1 cut off the conductive coating, the UHSC

J. Mater. Civ. Eng., 2019, 31(1): 04018357

Table 6. Results of the length and crack development speed of the main and branching cracks of Specimens 1, 2, and 3

Specimen	Time (ms)	L_{m1} (mm)	L_{m2} (mm)	L_b (mm)	v_{m2} (mm/ms)	v_b (mm/ms)
1	0	72.64	0.00	0.00	0.00	0.00
	15	72.64	0.74	0.12	46.25	7.12
	30	72.64	1.41	1.11	44.67	66.00
	45	72.64	3.89	5.74	165.33	308.67
	70	72.64	6.81	6.48	116.80	29.60
	90	72.64	10.33	9.89	176.00	170.50
	105	72.64	12.54	11.56	147.33	111.33
	120	72.64	13.21	12.15	44.67	39.33
	140	72.64	15.24	14.39	101.50	112.00
	160	72.64	19.11	16.74	193.50	117.50
	179	72.64	22.08	17.45	156.32	37.37
2	0	69.85	0.00	0.00	0.00	0.00
	15	69.85	0.58	0.21	30.53	11.05
	30	69.85	1.22	1.02	33.68	42.63
	45	69.85	4.32	5.28	163.16	224.21
	70	69.85	7.33	6.95	158.42	87.89
	90	69.85	9.98	9.28	139.47	122.63
	105	69.85	11.25	11.53	66.84	118.42
	120	69.85	14.02	12.91	145.79	72.63
	140	69.85	18.54	15.41	237.89	131.58
	160	69.85	21.71	16.01	166.84	31.58
	179	69.85	24.39	16.26	141.05	13.16
3	0	70.11	0.00	0.00	0.00	0.00
	15	70.11	0.92	0.18	48.42	9.47
	30	70.11	1.76	1.36	44.21	62.11
	45	70.11	4.07	6.11	121.58	250.00
	70	70.11	5.23	6.98	61.05	45.79
	90	70.11	9.59	9.17	229.47	115.26
	105	70.11	12.77	11.12	167.37	102.63
	120	70.11	15.13	12.86	124.21	91.58
	140	70.11	18.54	16.89	179.47	212.11
	160	70.11	21.09	17.55	134.21	34.74
	179	70.11	23.73	18.02	138.95	24.74

Note: L_b = length of the branching crack; L_{m1} = length of Main crack 1; L_{m2} = length of Main crack 2; v_b = crack development speed of the branching crack; and v_{m2} = crack development speed of Main crack 2.

recorded the development process of Main crack 2 and the branching crack. The length of Main crack 2 ranged from $L_{m2\cdot\min} = 0$ mm to $L_{m2\cdot\max} = 22.08$ mm, thereby showing an increasing trend with time. At approximately $t = 15$ ms, the branching crack appeared, with its length ranging from $L_{b\cdot\min} = 0$ mm to $L_{b\cdot\max} = 17.45$ mm. The maximum length of Main crack 2 was 26.53% longer than that of the branching crack. The crack length–time curve of Specimens 1–3 was obtained from the calculation results, and its plot is shown in Fig. 8. Notably, the overall trends of the two kinds of curves are similar. However, the crack length–time curve of the branching crack fluctuates more than that of Main crack 2. The branching crack consumed some of the fracture energy of Main crack 2, which helped Main crack 2 maintain a stable cracked condition, e.g., at approximately $t = 35$ to 75 ms. L_b exceeded L_{m2} in Specimen 1, and the maximum difference value was approximately 1.85 mm. The length–time curve of the branching crack mutated, whereas the length–time curve of Main crack 2 maintained stable growth. Specimen 2 and Specimen 3 had the same law.

The development speed of Main crack 2, v_{m2}, and the development speed of the branching crack, v_b, were calculated based on $v = s/t$, and the results for Specimens 1–3 are given in Table 6, where s is the crack length and t is the cracking time. For example, in Specimen 1, the development speed of Main crack 2 ranged from $v_{m2\cdot\min} = 0$ mm/ms to $v_{m2\cdot\max} = 193.5$ mm/ms.

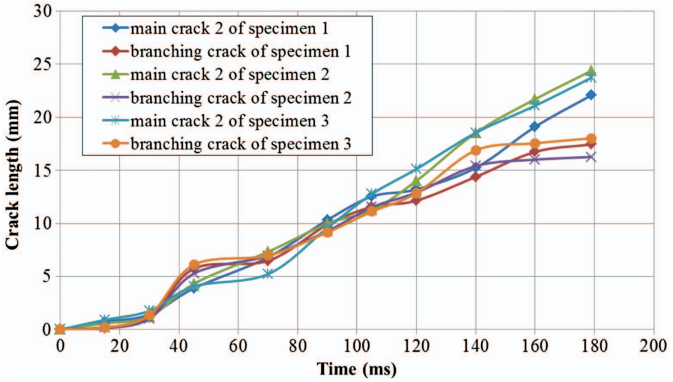

Fig. 8. (Color) Crack length–time curve of the specimen within 180 ms for Specimens 1, 2, and 3.

At approximately $t = 15$ ms, the branching crack appeared, and its development speed ranged from $v_{b\cdot\min} = 0$ mm/ms to $v_{b\cdot\max} = 308.67$ mm/ms. The maximum development speed of Main crack 2 was 37.31% slower than that of the branching crack. The crack development speed–time curve was obtained from the calculation results, and its plot is shown in Fig. 9. Notably, the overall trends of the two curves are still similar. Moreover, the development speed–time curves of the branching crack and Main crack 2 exhibited strong fluctuations. In Specimen 1 at approximately $t = 30$–60 ms and $t = 120$–140 ms, the development speed of the branching crack exceeded that of Main crack 2. In Specimen 1 at $t = 179$ ms, the branching crack connected to Main crack 1, and its development speed reached 0 mm/ms.

The trend lines of the two curves were also obtained based on the previous analysis. The slopes of the trend lines that correspond to Main crack 2 and the branching crack are $k_{m2} = 0.67$ and $k_b = 0.12$, respectively. This finding indicates the high rangeability of the speed change of the branching crack, which did not exhibit an evident increasing trend. Thus, the value of k_b is approximately 0. However, Main crack 2 maintained an increasing trend of development speed during the entire loading process. The value of k_{m2} is 5.58 times higher than that of the branching crack.

In Specimen 1 at $t = 45$ ms, the branching crack presented a maximum development speed of $v_{b\cdot\max} = v_{b\cdot t=45\text{ ms}} = 308.67$ mm/ms. This value is 86.70% higher than $v_{m2\cdot t=45\text{ ms}} = 165.33$ mm/ms. When Fig. 9 was compared with Fig. 8, the researchers determined that the length–time curve also mutated at approximately $t = 45$ ms. This finding indicated that at approximately $t = 45$ ms, the energy release process of the branching crack was dramatic. Thus, Main crack 2 could maintain a relatively stable cracking speed, i.e., the branching crack could absorb some of the energy of Main crack 2 and control the development of the main crack, thereby delaying the time to final damage. The same low can also be found in Specimens 2 and 3.

Conclusion

This study investigated the cracking behavior of main and branching cracks in concrete based on compression tests and a UHSC system. During the entire loading process, the main crack kept developing, whereas the branching crack lagged behind. The final length of the main crack was longer than that of the branching crack. The crack development speed range of the branching crack was higher than that of the main crack. The maximum development speed of the branching crack was also higher than that of the main crack.

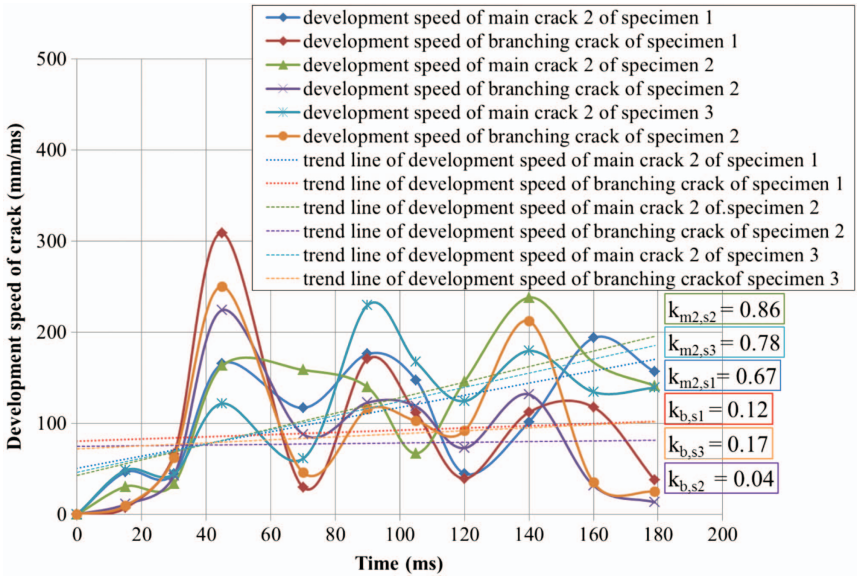

Fig. 9. (Color) Development speed–time curves of the main and branching cracks of Specimens 1, 2, and 3.

The length–time and development speed–time curves of the branching crack exhibited evident fluctuations compared with those of the main crack. The branching crack consumed some of the fracture energy of Main crack 2, thereby helping Main crack 2 maintain a stable cracked condition.

During the entire loading process, the main crack maintained a relatively stable crack development speed. This relatively stable speed may have benefited from the development of the branching crack. The results show that if the concrete is damaged, then the branching crack can delay the development speed of the main crack and minimize damage. A limitation of this testing procedure is that one UHSC can only shoot one surface of a concrete specimen, meaning the other five surfaces will be neglected. Occasionally, the shooting surface will have only a few cracks, whereas the other surfaces will have many cracks. This phenomenon will lead to a serious error, and the solution for this problem will be the subject of a future work. The authors only investigated the relationship between main and branching cracks based on compression, tensile, and bending tests, which will also be the subject of a future work.

Acknowledgments

This study was financially supported by the National Natural Science Foundation of China (Nos. 51722907, 51679197, and 51579207) and the National Science Foundation for Post-Doctoral Scientists of China (No. 2014M562524XB). The authors wish to thank the reviewers and editor for advice on this paper.

Notation

The following symbols are used in this paper:

k_b = slope of the trend line of the branching crack;
k_{m2} = slope of the trend line of Main crack 2;
L_b = length of the branching crack;
$L_{b\cdot\max}$ = maximum value of the branching crack;
$L_{b\cdot\min}$ = minimum value of the branching crack;
L_{m1} = length of Main crack 1;
L_{m2} = length of Main crack 2;
$L_{m2\cdot\max}$ = maximum value of the length of Main crack 2;
$L_{m2\cdot\min}$ = minimum value of the length of Main crack 2;
s = crack length;
t = cracking time;
v = crack development speed;
v_b = crack development speed of the branching crack;
$v_{b\cdot\max}$ = maximum value of the crack development speed of the branching crack;
$v_{b\cdot\min}$ = minimum value of the crack development speed of the branching crack;
$v_{b\cdot t=45\ \mathrm{ms}}$ = crack development speed of the branching crack at $t = 45$ mm;
v_{m2} = crack development speed of Main crack 2;
$v_{m2\cdot\max}$ = maximum value of the crack development speed of Main crack 2;
$v_{m2\cdot\min}$ = minimum value of the crack development speed of Main crack 2; and
$v_{m2\cdot t=45\ \mathrm{ms}}$ = crack development speed of Main crack 2 at $t = 45$ mm.

References

Aggelis, D. G., S. Verbruggen, E. Tsangouri, T. Tysmans, and D. V. Hemelrijck. 2013. "Characterization of mechanical performance of concrete beams with external reinforcement by acoustic emission and digital image correlation." *Constr. Build. Mater.* 47 (5): 1037–1045. https://doi.org/10.1016/j.conbuildmat.2013.06.005.

Agoramoorthy, G. 2015. "The future of India's obsolete dams: Time to review their safety and structural integrity." *Futures* 67: 22–25. https://doi.org/10.1016/j.futures.2015.02.001.

Damasceno, I. I. R., M. P. Ferreira, and D. R. C. Oliveira. 2013. "RC beams with steel fibers under impact loads." *Acta Sci. Technol.* 36 (1): 23–31. https://doi.org/10.4025/17561.

Destrebecq, J.-F., E. Toussaint, and E. Ferrier. 2011. "Analysis of cracks and deformations in a full scale reinforced concrete beam using a digital image correlation technique." *Exp. Mech.* 51 (6): 879–890. https://doi.org/10.1007/s11340-010-9384-9.

Faella, C., C. Lima, E. Martinelli, M. Pepe, and R. Realfonzo. 2016. "Mechanical and durability performance of sustainable structural

concretes: An experimental study." *Cem. Concr. Compos* 71: 85–96. https://doi.org/10.1016/j.cemconcomp.2016.05.009.

Forquin, P. 2012. "An optical correlation technique for characterizing the crack velocity in concrete." *Eur. Phys. J.-Spec. Top* 206 (1): 89–95. https://doi.org/10.1140/epjst/e2012-01590-6.

Galouei, M., and A. Fakhimi. 2015. "Size effect, material ductility and shape of fracture process zone in quasi-brittle materials." *Comput. Geotech.* 65: 126–135. https://doi.org/10.1016/j.compgeo.2014.12.010.

Gao, G., S. Huang, K. Xia, and Z. Li. 2015. "Application of digital image correlation (DIC) in dynamic notched semi-circular bend (NSCB) tests." *Exp. Mech.* 55 (1): 95–104. https://doi.org/10.1007/s11340-014-9863-5.

Gary, G., and P. Bailly. 1998. "Behaviour of quasi-brittle material at high strain rate. Experiment and modeling." *Eur. J. Mech., A/Solids* 17 (3): 403–420. https://doi.org/10.1016/S0997-7538(98)80052-1.

Küntz, M., M. Jolin, J. Bastien, F. Perez, and F. Hild. 2006. "Digital image correlation analysis of crack behavior in a reinforced concrete beam during a load test." *Can. J. Civ. Eng.* 33 (11): 1418–1425. https://doi.org/10.1139/l06-106.

Lai, J. X., S. Y. He, J. L. Qiu, J. X. Chen, L. X. Wang, K. Wang, and J. B. Wang. 2017. "Characteristics of seismic disasters and aseismic measures of tunnels in Wenchuan earthquake." *Environ. Earth Sci.* 76: 94. https://doi.org.10.1007/s12665-017-6405-3.

Lai, J. X., X. L. Wang, J. L. Qiu, G. Z. Zhang, J. X. Chen, Y. L. Xie, and Y. B. Luo. 2018. "A state-of-the-art review of sustainable energy based freeze proof technology for cold-region tunnels in China." *Renewable Sustainable Energy Rev.* 82 (3): 3554–3569. https://doi.org/10.1016/j.rser.2017.10.104.

Lawn, B. 1993. *Fracture of brittle solids*. Cambridge, UK: Cambridge University Press.

Li, J. Z., Z. J. Lv, H. S. Zhang, and F. L. Huang. 2013. "Perforation experiments of concrete targets with residual velocity measurements." *Int. J Impact Eng.* 57 (1): 1–6. https://doi.org/10.1016/j.ijimpeng.2013.01.007.

Li, Q. B., J. F. Guan, Z. M. Wu, W. Dong, and S. W. Zhou. 2016. "Equivalent maturity for ambient temperature effect on fracture parameters of site-casting dam concrete." *Constr. Build. Mater.* 120: 293–308. https://doi.org/10.1016/j.conbuildmat.2016.05.111.

Li, W., M. P. Ghaz, J. Castro, and J. Weiss. 2012. "Water absorption and critical degree of saturation relating to freeze-thaw damage in concrete pavement joints." *J. Mater. Civ. Eng.* 24 (3): 299–307. https://doi.org/10.1061/(ASCE)MT.1943-5533.0000383.

Matthes, J., J. Hock, P. Waibel, A. Scherrmann, H.-J. Gehrmann, and H. B. Keller. 2016. "A high-speed camera based approach for the on-line analysis of particles in multi-fuel burner flames." *Exp. Therm. Fluid Sci.* 73: 10–17. https://doi.org/10.1016/j.expthermflusci.2015.08.017.

Nunes, L. C. S., and J. M. L. Reis. 2012. "Estimation of crack-tip-opening displacement and crack extension of glass fiber reinforced polymer mortars using digital image correlation method." *Mater. Des.* 33 (1): 248–253. https://doi.org/10.1016/j.matdes.2011.07.051.

Oey, T., J. Stoian, J. L. Li, C. Vong, M. Balonis, A. Kumar, W. Franke, and G. Sant. 2014. "Comparison of $Ca(NO_3)_2$ and $CaCl_2$ admixtures on reaction, setting, and strength evolutions in plain and blended cementing formulations." *J. Mater. Civ. Eng.* 27 (10): 04014267. https://doi.org/10.1061/(ASCE)MT.1943-5533.0001240.

Palankar, N., A. U. R. Shankar, and B. M. Mithun. 2016. "Durability studies on eco-friendly concrete mixes incorporating steel slag as coarse aggregates." *J. Clean. Prod.* 129: 437–448. https://doi.org/10.1016/j.jclepro.2016.04.033.

Pichler, B., and C. Hellmich. 2011. "Upscaling quasi-brittle strength of cement paste and mortar: A multi-scale engineering mechanics model." *Cem. Concr. Res.* 41 (5): 467–476. https://doi.org/10.1016/j.cemconres.2011.01.010.

Pyo, S., M. Alkaysi, and S. E. Tawil. 2016. "Crack propagation speed in ultra high performance concrete (UHPC)." *Constr. Build. Mater.* 114: 109–118. https://doi.org/10.1016/j.conbuildmat.2016.03.148.

Qin, Y., J. R. Chai, and F. N. Dang. 2013. "Improved random aggregate model for numerical simulations of concrete engineering simulations of concrete engineering." *J. Civ. Eng. Manage.* 19 (2): 285–295. https://doi.org/10.3846/13923730.2012.760481.

Qin, Y., J. R. Chai, W. H. Ding, F. N. Dang, M. Lei, and Z. G. Xu. 2016. "A quasi real-time approach to investigating the damage and fracture process in plain concrete by X-ray tomography." *J. Civ. Eng. Manage.* 22 (6): 792–799. https://doi.org/10.3846/13923730.2014.914089.

Qiu, J., X. Wang, J. Lai, Q. Zhang, and J. Wang. 2018a. "Response characteristics and preventions for seismic subsidence of loess in northwest China." *Nat. Hazards* 92 (7): 1–27. https://doi.org/10.1007/s11069-018-3272-5.

Qiu, J. L., H. Q. Liu, J. X. Lai, H. P. Lai, J. X. Chen, and K. Wang. 2018b. "Investigating the long term settlement of a tunnel built over improved loessial foundation soil using jet grouting technique." *J. Perform. Constr. Facil.* 32 (5): 04018066. https://doi.org/10.1061/(ASCE)CF.1943-5509.0001155.

Reu, P. L., and T. J. Miller. 2008. "The application of high-speed digital image correlation." *J. Strain Anal. Eng.* 43 (8): 673–688. https://doi.org/10.1243/03093247JSA414.

Scalici, T., V. Fiore, G. Orlando, and A. Valenza. 2015. "A DIC-based study of flexural behaviour of roving/mat/roving pultruded composites." *Compos. Struct.* 131: 82–89. https://doi.org/10.1016/j.compstruct.2015.04.058.

Soumya Pandey, A. D., R. Das, M. J. Mahesh, S. Anvesh, and P. Saini. 2016. "Structural analysis of a historical dam." *Procedia Eng.* 144: 140–147. https://doi.org/10.1016/j.proeng.2016.05.017.

Tarefder, R. A., and M. Ahmad. 2015. "Evaluating the relationship between permeability and moisture damage of asphalt concrete pavements." *J. Mater. Civ. Eng.* 27 (5): 04014172. https://doi.org/10.1061/(ASCE)MT.1943-5533.0001129.

Ueno, H., M. Beppu, and A. Ogawa. 2017. "A method for evaluating the local failure of short polypropylene fiber-reinforced concrete plates subjected to high-velocity impact with a steel projectile." *Int. J. Impact Eng.* 105: 68–79. https://doi.org/10.1016/j.ijimpeng.2016.08.008.

Unosson, M., and L. Nilsson. 2006. "Projectile penetration and perforation of high performance concrete: Experimental results and macroscopic modeling." *Int. J Impact Eng.* 32 (7): 1068–1085. https://doi.org/10.1016/j.ijimpeng.2004.11.003.

Wang, S. S., H. T. N. Le, L. H. Poh, H. J. Feng, and M. H. Zhang. 2016. "Resistance of high-performance fiber-reinforced cement composites against high-velocity projectile impact." *Int. J Impact Eng.* 95: 89–104. https://doi.org/10.1016/j.ijimpeng.2016.04.013.

Wu, H., Q. Fang, Y. Peng, Z. M. Gong, and X. Z. Kong. 2015. "Hard projectile perforation on the monolithic and segmented RC panels with a rear steel liner." *Int. J Impact Eng.* 76: 232–250. https://doi.org/10.1016/j.ijimpeng.2014.10.010.

Wu, Y., S. L. Xu, Q. H. Li, G. Ruiz, and R. C. Yu. 2016. "Estimation of real fracture parameters of a dam concrete with large size aggregates through wedge splitting tests of drilled cylindrical specimens." *Eng. Fract. Mech.* 163: 23–36. https://doi.org/10.1016/j.engfracmech.2016.06.012.

Wu, Z. M., R. Hua, J. J. Zheng, F. Xu, and W. Dong. 2011. "An experimental investigation on the FPZ properties in concrete using digital image correlation technique." *Eng. Fract. Mech.* 78 (17): 2978–2990. https://doi.org/10.1016/j.engfracmech.2011.08.016.

Xu, S. L., J. Y. Huang, P. F. Wang, C. Zhang, L. J. Zhou, and S. S. Hu. 2015. "Investigation of rock material under combined compression and shear dynamic loading: An experimental technique." *Int. J Impact Eng.* 86 (7): 206–222. https://doi.org/10.1016/j.ijimpeng.2015.07.014.

Yang, H. M., Z. He, Y. X. Shao, and L. Li. 2018. "Improving freeze-thaw resistance and strength gain of roller compacted fly ash concretes with modified absorbent polymer." *J. Mater. Civ. Eng.* 30 (3): 04018010. https://doi.org/10.1061/(ASCE)MT.1943-5533.0002159.

Yao, Y., F. A. Silva, M. Butler, V. Mechtcherine, and B. Mobasher. 2015. "Tension stiffening in textile-reinforced concrete under high speed tensile loads." *Cem. Concr. Compos.* 64: 49–61. https://doi.org/10.1016/j.cemconcomp.2015.07.009.

Yu, R., P. Spiesz, and H. J. H. Brouwers. 2016. "Energy absorption capacity of a sustainable ultra-high performance fibre reinforced concrete (UHPFRC) in quasi-static mode and under high velocity projectile impact." *Cem. Concr. Compos.* 68: 109–122. https://doi.org/10.1016/j.cemconcomp.2016.02.012.

Zhang, Q. B., and J. Zhao. 2013. "Determination of mechanical properties and full-field strain measurements of rock material under dynamic loads." *Int. J. Rock Mech. Min.* 60 (8): 423–439. https://doi.org/10.1016/j.ijrmms.2013.01.005.

Zhou, Y., B. Gencturk, K. Willam, and A. Attar. 2014. "Carbonation-induced and chloride-induced corrosion in reinforced concrete structures." *J. Mater. Civ. Eng.* 27 (9): 04014245. https://doi.org/10.1061/(ASCE)MT.1943-5533.0001209.

Zhou, Z. L., Y. Zhao, Y. H. Jiang, Y. Zou, X. Cai, and D. Y. Li. 2017. "Dynamic behavior of rock during its post failure stage in SHPB tests." *T. Nonferr. Metal. Soc.* 27 (1): 184–196. https://doi.org/10.1016/S1003-6326(17)60021-9.